



Research paper

Analytical modeling and experimental validation of rotationally actuated pinned–pinned and fixed–pinned buckled beam bistable mechanisms

Loïc Tissot-Daguette^{*}, Hubert Schneegans, Etienne Thalmann, Simon Henein

Micromechanical and Horological Design Laboratory (Instant-Lab), École Polytechnique Fédérale de Lausanne (EPFL), Rue de la Maladière 71c, Neuchâtel, 2000, NE, Switzerland



ARTICLE INFO

Keywords:

Beam buckling
Bistable mechanism
Snap-through
Theoretical modeling

ABSTRACT

Buckled beams have become key building blocks in compliant mechanisms to achieve nonlinear behaviors, such as bistability, constant-force and stiffness tuning. However, designing and modeling such components is challenging due to their highly nonlinear characteristics and existing models typically lack accuracy or rely on numerical computations. This paper aims at giving closed-form formulas to efficiently characterize the snap-through behavior and facilitate the design process of rotationally actuated pinned–pinned and fixed–pinned bistable buckled beams. A new generic analytical model for precompressed beams based on Euler–Bernoulli beam theory is first established and then applied to these two configurations. Finite element and experimental validations are performed, showing excellent agreement with the model. The results show that the angular input at the pinned beam extremity is significantly decoupled from the angular or moment output at the other extremity, until snap-through. Additionally, we show that the stable output values can be controlled by adjusting the precompression displacement of the buckled beam. Finally, we demonstrate the practicality of the studied building blocks and their modeling on a novel bistable gripper design.

1. Introduction

Bistable mechanisms have the ability to maintain two specific distinct positions without the necessity of external power; energy is only required when switching from one stable position to the other. These mechanisms are highly beneficial for microelectromechanical systems (MEMS), such as electrical [1] or photonic [2] microswitches, microvalves [3], mechanical non-volatile memory [4], and energy harvesters [5]. At micro- and nano-scale, bistable mechanisms usually rely on the geometrical nonlinearity of buckled beams in order to be compatible with monolithic microfabrication techniques. The precompression of the beam can be achieved either by a prescribed compression displacement along the axial direction [6,7], or through residual stress created by heating or oxidation during the manufacturing process [5,8]. Alternatively, the beam can be preshaped in one of its two stable deflections, which greatly simplifies the fabrication and suppresses the need for axial preloading [9]. However, this creates an asymmetry in the actuation characteristics. These bistable buckled beams can be used as building blocks for bistable flexure mechanisms [10] and even be combined serially to create multistable mechanisms [11].

Despite the wide interest in bistable mechanisms based on buckled beams, their modeling remains challenging due to their highly nonlinear characteristics, such as bifurcations and hysteresis. A first Lagrangian approach based on Euler–Bernoulli beam theory was

^{*} Corresponding author.

E-mail addresses: loic.tissot-daguette@epfl.ch (L. Tissot-Daguette), hubert.schneegans@epfl.ch (H. Schneegans), etienne.thalmann@epfl.ch (E. Thalmann), simon.henein@epfl.ch (S. Henein).

<https://doi.org/10.1016/j.mechmachtheory.2022.104874>

Received 18 January 2022; Received in revised form 1 April 2022; Accepted 2 April 2022

Available online 30 April 2022

0094-114X/© 2022 The Author(s). Published by Elsevier Ltd. This is an open access article under the CC BY license (<http://creativecommons.org/licenses/by/4.0/>).

conducted by Vangbo [12] to model fixed–fixed buckled beams with lateral force actuation at their center. His analytical model assumed small deformations and that the deflection of the beam is a superposition of its equilibrium shapes (also called buckling modes). The force–displacement curve was obtained by minimizing the total energy of the system with the method of Lagrange multipliers. Bifurcation points, constant negative stiffness region and snap-through behavior were formulated to help the design of such buckled beams. Qiu et al. [9] applied the Lagrangian method on curved beams with center actuation. The authors assumed that a finite superposition of the three first modes is enough to significantly characterize the force–displacement curve. This assumption was validated by finite element method (FEM) and experiments. Later, Cazottes et al. [13] used the same approach to analyze off-center actuations of buckled beams with fixed ends. Unlike in the case of center actuation, their model revealed hysteresis phenomena in the actuation force–displacement curve. They also demonstrated a good agreement with experiments if a sufficient number of first buckling modes is considered. Hussein and al. [14] showed the importance of high buckling modes in the derivation of the beam internal stresses using the Lagrangian method. Yan et al. [15] then provided simple formulas for the critical force and displacement values, for center and off-center force actuation.

Numerical approaches to the problem were also explored. Zhao et al. [16], developed a large deformation model with numerical approximations to characterize the actuation of fixed–guided inclined beams. Holst and al. [17] then formulated the deflection of such beams in terms of elliptic integrals evaluated numerically. Alternatively, Camescasse et al. [18,19] derived and validated experimentally an elastica model to consider large deflections of pinned–pinned buckled beams actuated by central and non-central external forces.

In this paper, we propose a new way of modeling bistable buckled beams that overcomes the drawbacks of the Lagrangian approach and the large deflection models. Indeed, the Lagrangian methods are only accurate for small deformations of the beam and their accuracy depends on the number of buckling modes considered. In contrast, elliptic integral methods are very accurate, as they consider large deformations of the beam, but need numerical computations which prevents the derivation of closed-form expressions that can be directly used for the design. In our previous work, we developed a new analytical approach, based on Euler–Bernoulli beam theory, to model and design two specific mechanisms: (1) a constant-force surgical tool based on beam buckling [20] and (2) a stiffness tuning load cell based on a preloaded beam [21]. In this paper, we first generalize this analytical model in order to model and design precompressed beams with different boundary conditions and actuation modes. We then apply this generic approach to pinned–pinned and fixed–pinned buckled beams that are rotationally actuated at one pinned end. These mechanisms have the advantage of decoupling the input actuation from the output angular motion or moment. Such mechanisms have already been studied [10,22], but existing models fail to fully describe the behavior of the buckled beams and lack simple formulas for their design. In contrast, our model provides practical tools for the design of such mechanisms, in the form of explicit analytical expressions and normalized graphs for the actuation characteristics, strain energy, and internal stress of the beam. All our analytical results are validated by FEM simulations or experiments. In addition to this, the practicality of our new analytical method is demonstrated by designing and modeling a bistable gripper based on pinned–pinned and fixed–pinned buckled beams.

In summary, the main contributions of this paper are:

1. a generic analytical model of precompressed beams based on Euler–Bernoulli beam theory;
2. closed-form analytical formulas and normalized graphs to design pinned–pinned and fixed–pinned bistable buckled beam mechanisms actuated by a moment or an angle;
3. a validation of the presented analytical model by FEM simulations and experimental testing;
4. a gripper design example demonstrating the benefits of such bistable mechanisms.

The pinned–pinned and fixed–pinned buckled beam mechanisms are described in Section 2. Their theoretical modeling is conducted in Section 3. FEM and experimental methods to validate the analytical model are presented in Section 4. A synthesis of the results is showcased and discussed in Section 5. An example of application of these mechanisms is given in Section 6. Concluding remarks and future works are addressed in Section 7.

2. Description of the mechanisms

We consider two rotationally driven bistable mechanisms where the bistability comes from: (1) a pinned–pinned buckled beam; (2) a fixed–pinned buckled beam. Their schematics are presented in Figs. 1 and 2. The mechanisms have an input pivot situated at the right beam extremity, where a moment M_{in} can be applied. For the pinned–pinned configuration, the output is the rotation angle θ_{out} of the left pivot. For the fixed–pinned configuration, the output is the reaction moment M_{out} applied to the fixed support.

For both mechanisms, the beam is considered initially straight (when the beam is stress free), slender and inextensible (Figs. 1a and 2a). All the pin-joints are assumed to rotate without friction, parasitic motion or restoring torque, and their axis of rotation coincides with the corresponding beam extremity.

A preloading stage, made of a position-controlled slider placed at the right extremity, is used to shorten the distance between the beam's ends by a displacement Δl . This axial precompression causes the beam to buckle into one of its two stable positions (Figs. 1b and 2b). The initial length of the beam is L and the horizontal projection of the beam length is denoted l and is equal to $L - \Delta l$. In Figs. 1c and 2c, the buckled beam is actuated in rotation at the input pivot (by a controlled moment M_{in} or by a controlled angle θ_{in}) to switch between the stable positions of the mechanism. The precompression displacement Δl is considered constant during the actuation. The output pivot angle θ_{out} and the output reaction moment M_{out} (for the pinned–pinned and fixed–pinned configurations, respectively) are functions of the input actuation. The relation between the input and output characteristics, as well as the snap-through behavior during state switching of these two mechanisms, will be modeled analytically in the next section.

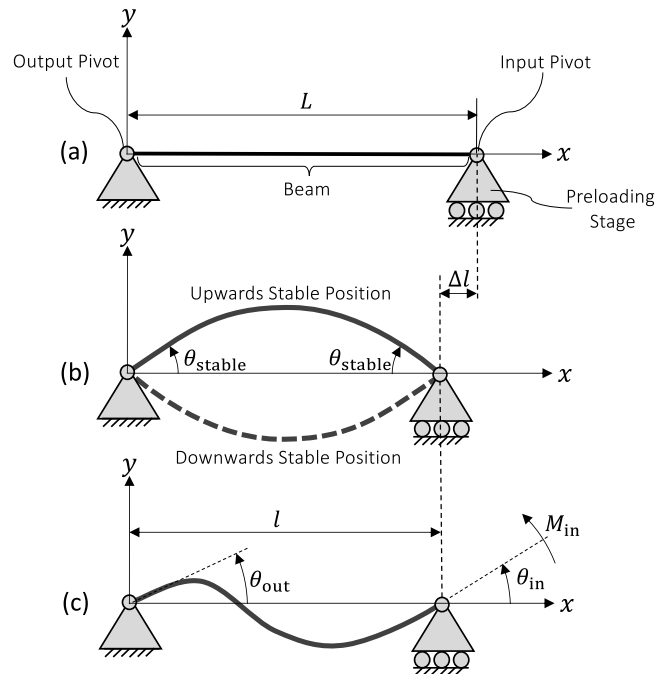


Fig. 1. Pinned–pinned buckled beam (a) as-fabricated, (b) buckled into one of its two stable positions using the preloading stage, and (c) where a moment is applied to the input pivot to switch between the stable states.

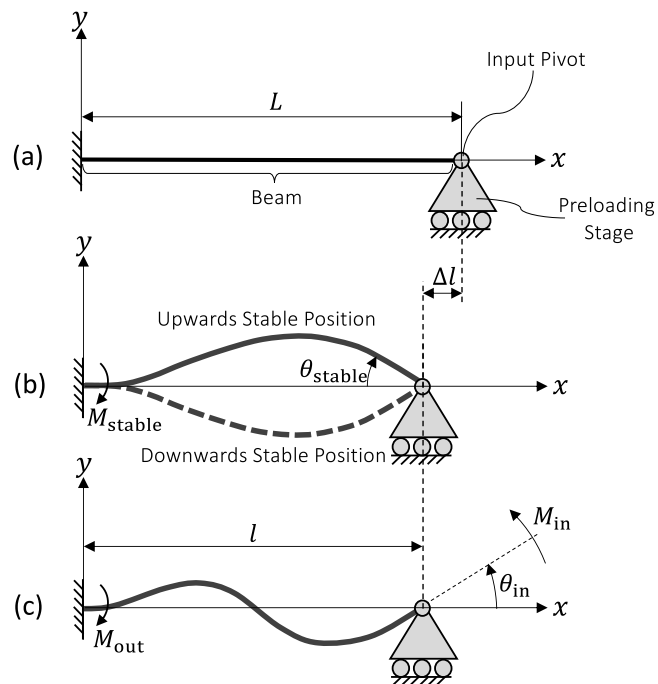


Fig. 2. Fixed–pinned buckled beam (a) as-fabricated, (b) buckled into one of its two stable positions using the preloading stage, and (c) where a moment is applied to the input pivot to switch between the stable states.

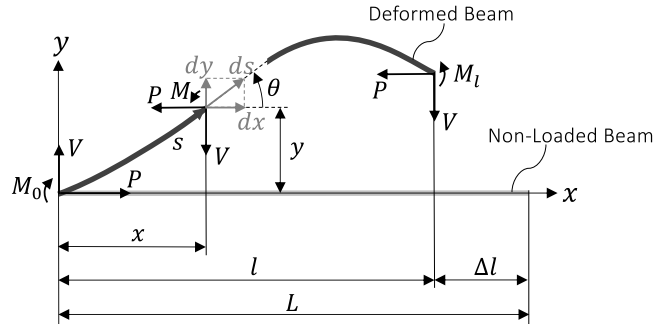


Fig. 3. Deflection diagram and variables of a generic axially precompressed beam.

3. Theoretical modeling

In this section, a generic analytical model for precompressed beams is developed. This theoretical model allows to determine the actuation characteristics of the pinned–pinned and fixed–pinned buckled beam bistable mechanisms described in Section 2. Furthermore, it enables the derivation of simple formulas and normalized graphs for the design of such mechanisms.

3.1. Generic analytical model of precompressed beams

First, we introduce the general theoretical model of axially precompressed beams derived from Euler–Bernoulli beam theory. It is assumed that the elastic behavior of the beam is linear and homogeneous, that the influence of gravity is negligible, and that dynamic effects can be ignored. The reference frame is placed such that its origin coincides with the left extremity of the beam, see Fig. 3. The x -axis is coaxial with the undeflected beam axis and the y -axis is perpendicular to it. For a given arclength coordinate s , we can evaluate the beam angle θ , the bending moment M , the shear force V and the compressive force P . The moments $M_0 = M(s = 0)$ and $M_l = M(s = L)$ stand respectively for the reaction moments at the left and right beam extremities.

Assuming small beam deflection angles, $\theta \cong dy/ds$, the Euler–Bernoulli moment–curvature relationship can be expressed as:

$$M(s) \cong EI \frac{d^2y(s)}{ds^2} \tag{1}$$

where EI stands for the flexural rigidity of the beam. The bending moment $M(s)$ is related to the beam reactions as follows:

$$M(s) = -Py(s) + Vx(s) + M_0 \tag{2}$$

Equalizing Eqs. (1) and (2), results in a differential equation which can only be solved with numerical methods [16–18,23–26]. To obtain closed-form solutions to the differential equation, we propose to linearize $x(s)$ with the approximation:

$$x(s) \cong \frac{l}{L}s \tag{3}$$

Note that this linearization satisfies the boundary conditions $x(s = 0) = 0$ and $x(s = L) = l$. Unlike Lagrangian-based methods [9,12–15,27–30], where s is directly approximated by x , Eq. (3) will allow to distinguish the use of the initial length L from the projected length l in the analytical formulas describing precompressed beams.

Using the boundary condition $y(s = 0) = 0$, the differential equation from Eqs. (1) and (2), with the substitution of the linearization (3), results in the general solution:

$$y(s) = A \sin(ks) + B(\cos(ks) - 1) + Cs \tag{4}$$

where:

$$k = \sqrt{\frac{P}{EI}} \tag{5}$$

$$B = -\frac{M_0}{P} \tag{6}$$

$$C = \frac{V}{P} \frac{l}{L} \tag{7}$$

Upon the substitution of Eq. (3) into Eq. (4), the beam deflection can be expressed as a function of the horizontal coordinate x :

$$y(x) = A \sin\left(kL\frac{x}{l}\right) + B\left(\cos\left(kL\frac{x}{l}\right) - 1\right) + CL\frac{x}{l} \tag{8}$$

Since we assume that the beam contraction due to the axial load P is negligible compared to the preload displacement Δl , the total arclength of the beam is equal to its initial length L . Therefore, the horizontal projected length l can be integrated as follows:

$$l = \int_0^L \cos(\theta) ds \tag{9}$$

As small deflection angles are assumed, the first two terms of the power series expansion $\cos(\theta) \cong 1 - \theta^2/2 \cong 1 - (dy/ds)^2/2$ yields the preload displacement:

$$\Delta l = L - l = \frac{1}{2} \int_0^L \left(\frac{dy}{ds} \right)^2 ds \tag{10}$$

Substituting the differentiation of Eq. (4) with respect to s in Eq. (10), the integral results in the following constraint:

$$\begin{aligned} \Delta l = & \frac{(A^2 + B^2)(kL)^2}{4L} + \frac{(A^2 - B^2)kL \sin(2kL)}{8L} + \frac{ABkL(\cos(2kL) - 1)}{4L} \\ & + \frac{C^2L}{2} + AC \sin(kL) + BC(\cos(kL) - 1) \end{aligned} \tag{11}$$

Based on the load case, the deflection parameters A , B and C can now be determined using Eqs. (4)–(7) and (11), knowing the boundary conditions of the beam and the precompression displacement. Note that the product kL is a non-dimensional parameter that expresses the compression state of the beam. As we will see in the next sections, this parameter has specific values when the beam is at equilibrium (i.e., when no external actuation is applied). It can also be varied to plot parametric load–displacement curves that are useful for analyzing the transition between equilibrium states. Once the deflection parameters are obtained, we can compute the strain energy and the maximum internal stress of the beam, respectively:

$$\begin{aligned} E_{\text{strain}} = & \frac{EI}{2} \int_0^L \left(\frac{d^2y}{ds^2} \right)^2 ds \\ = & \frac{EI}{L^2} (kL)^3 \left(\frac{(A^2 + B^2)kL}{4L} - \frac{(A^2 - B^2) \sin(2kL)}{8L} - \frac{AB(\cos(2kL) - 1)}{4L} \right) \end{aligned} \tag{12}$$

$$\begin{aligned} \sigma_{\text{max}} = & \frac{\max(|M(s)|)h}{2I} \\ = & \frac{Eh}{2L^2} (kL)^2 \max \left(\left| A \sin \left(kL \frac{s}{L} \right) + B \cos \left(kL \frac{s}{L} \right) \right| \right), \quad \text{with } s \in [0, L] \end{aligned} \tag{13}$$

where h stands for the beam thickness.

Remark 1. Computing the strain energy of a beam is useful to analyze its stable and unstable deflections. It can also be used to evaluate the amount of energy stored (or released) during a given actuation.

Remark 2. The maximum stress formula allows to verify that the yield stress of the beam material is not exceeded. Since in this model we assume a slender and inextensible beam, the stress due to the axial compression $\sigma_{\text{comp}} = P/(bh)$, where b is the beam out-of-plane width, is neglected with respect to the bending stress [14].

3.2. Pinned–pinned buckled beam

3.2.1. Modeling

In this section, we model the pinned–pinned buckled beam mechanism using the formulas from the generic analytical model of Section 3.1. Applying the pinned–pinned boundary conditions, i.e., $y(s = L) = 0$ and $M_0 = 0$ to Eqs. (4) and (6) yields:

$$B = 0 \tag{14}$$

$$C = -\frac{A}{L} \sin(kL) \tag{15}$$

The pinned–pinned buckled beam deflection can then be expressed as a function of s and x , respectively:

$$y(s) = A \left(\sin \left(kL \frac{s}{L} \right) - \sin(kL) \frac{s}{L} \right) \tag{16}$$

$$y(x) = A \left(\sin \left(kL \frac{x}{l} \right) - \sin(kL) \frac{x}{l} \right) \tag{17}$$

Substituting Eqs. (14) and (15) into Eq. (11), the deflection parameter A can be expressed as a function of the free parameter kL :

$$A = \pm 2L \sqrt{\frac{\Delta l}{L} \left[(kL)^2 + kL \frac{\sin(2kL)}{2} + \cos(2kL) - 1 \right]^{-\frac{1}{2}}} \tag{18}$$

The input moment can be obtained by substituting the second differentiation of Eq. (16) with respect to s into Eq. (1) and evaluating it at $s = L$, yielding:

$$M_{\text{in}} = M(s = L) = -\frac{EI}{L} \frac{A}{L} (kL)^2 \sin(kL) \quad (19)$$

Considering $\theta \cong dy/ds$, the input and output angles follow from differentiating Eq. (16) with respect to s :

$$\theta_{\text{in}} = \theta(s = L) = \frac{A}{L} (kL \cos(kL) - \sin(kL)) \quad (20)$$

$$\theta_{\text{out}} = \theta(s = 0) = \frac{A}{L} (kL - \sin(kL)) \quad (21)$$

The strain energy of the pinned–pinned beam can be calculated from Eq. (12):

$$E_{\text{strain}} = \frac{1}{4} \frac{EI}{L} \left(\frac{A}{L} \right)^2 (kL)^3 \left(kL - \frac{\sin(2kL)}{2} \right) \quad (22)$$

Since the curved coordinate s takes any value between 0 and L , the maximum bending stress in the beam, given by Eq. (13), is:

$$\sigma_{\text{max}} = \frac{Eh}{2L} \frac{|A|}{L} (kL)^2 \cdot \begin{cases} \sin(kL), & 0 \leq kL < \frac{\pi}{2} \\ 1, & kL \geq \frac{\pi}{2} \end{cases} \quad (23)$$

3.2.2. Equilibrium positions

Equilibrium deflections of the beam occur, by definition, when the input moment M_{in} is equal to zero. Since we consider deflected beams, $A \neq 0$ in Eq. (16) and solving Eq. (19) leads to specific values for the parameter kL :

$$(kL)_{\text{equi}} = m\pi, \quad m = 1, 2, 3, \dots \quad (24)$$

where m is generally called the buckling mode. If $m = 1$, the beam is in its first buckling mode, $m = 2$ corresponds to the second buckling mode, etc. The deflection parameter A always having two opposite solutions, see Eq. (18), all modes have two symmetrical deflections. With global minimum energy, see Eq. (22), the two first mode solutions are the only stable equilibriums of the pinned–pinned buckled beam bistable mechanism. In stable state, the magnitude of the angles at both beam ends are equal and can be calculated using Eqs. (20), (21) and (24):

$$\theta_{\text{stable}} = |\theta_{\text{in}}(kL = \pi)| = |\theta_{\text{out}}(kL = \pi)| = 2\sqrt{\frac{AI}{L}} \quad (25)$$

Remark 3. Note that, for each mode, the input and output pivots of the pinned–pinned buckled beam have the same equilibrium angle (in absolute value), see Eqs. (20), (21) and (24).

3.2.3. Actuation characteristics

Using an actuation on the input pivot, we can switch the stable state of the pinned–pinned buckled beam mechanism. The actuation characteristics are plotted in Fig. 4. Parametric curves of the input moment (Eq. (19)), the output angle (Eq. (21)) and the strain energy (Eq. (22)), as a function of the input angle (Eq. (20)) are plotted in Figs. 4a, 4b and 4c, respectively. The free parameter kL is varied from 0 (no compressive force in Eq. (5)) to 2π (second mode). The two symmetrical branches, which we call *Branch 1* and *Branch 2*, correspond to the two opposite solutions of parameter A in Eq. (18). They are plotted together to display the possible snap-through transitions, i.e., unidirectional jumps from one branch to the other. Depending on the actuation type of the input pivot, i.e., angle control or moment control, the system will follow different paths and will snap at different limit points. We describe below examples for these two cases using Fig. 4 in order to demonstrate its practicality.

We can, for instance, describe how the mechanism reacts to a moment control at the input to switch its stable position from one stable position corresponding to the first mode (FM1) to the other symmetric one (FM2). From point FM1, by applying an increasing input moment the input angle increases until the system reaches the moment limit point ML1, see Fig. 4a. At this point, there are no other solutions on the current branch (Branch 1) if the input moment continues to rise (limit point instability). A solution (ML1') on the other branch (Branch 2) exists, leading to a snap-through from Branch 1 to Branch 2, as shown by the horizontal line of arrows on Fig. 4a. Note that the point ML1' is not on our calculated Branch 2 but on an extrapolated line from the zero compression point (ZC2), because the beam is in tension at ML1' and our model only considers a compressive axial force P . After snap-through, the moment input can be decreased until returning to zero as the mechanism stabilizes at point FM2. Note that, as the system goes from ML1' to FM2 along Branch 2, the beam axial load P changes sign when passing through ZC2 (transition from tensile to compressive load).

In the case of input angle control, the system will follow the same path from points FM1 to ML1 as for a moment control. However, after passing point ML1, the input moment will decrease as the input angle continues to increase, see Fig. 4a. When an angle limit point AL1 is reached, the mechanism will snap from Branch 1 to Branch 2 since no other solution exists with a larger input angle on Branch 1. This is shown by a vertical line of arrows on Fig. 4a. The system ends up at the post-snap point AL1' where the input angle can be decreased to reach the second stable position FM2.

For both moment and angle controls, after snap-through has occurred from Branch 1 to Branch 2, we can symmetrically reverse the direction of the actuation to snap back to Branch 1 following a symmetrical but different path (due to hysteresis). Since moment

and angle limits are encountered before the second mode points (SM1 and SM2), for both moment and angle controls, the second and thus higher modes are never reached. For readability, and since all the points of the moment control path are also reached by angle control, we only display angle control snap-through for the other actuation graphs (Figs. 4b and 4c).

Numerically, the input moment magnitude at moment limit points ML1 and ML2, denoted $M_{in,lim}$, corresponds to the maximum of the function $M_{in}(kL)$ (Eq. (19)) for $\pi \leq kL \leq 2\pi$ (i.e., between the first and second modes), namely when $kL = 1.58\pi$:

$$M_{in,lim} = 10.28 \frac{EI}{L} \sqrt{\frac{\Delta l}{L}} \quad (26)$$

The input angle magnitude at angle limit points AL1 and AL2, denoted $\theta_{in,lim}$, is the maximum of $\theta_{in}(kL)$ in Eq. (20) for $\pi \leq kL \leq 2\pi$, and is obtained when $kL = 1.92\pi$:

$$\theta_{in,lim} = 2.07 \sqrt{\frac{\Delta l}{L}} \quad (27)$$

Fig. 4b presents the graph of the output angle as a function of the input angle. In this figure, we can note that the output angle reaches a maximum magnitude (points MOA1 and MOA2) under input angle control when switching branches. This maximum output angle is obtained when $kL = 1.56\pi$ in Eq. (21) and is equal to:

$$\theta_{out,max} = 2.56 \sqrt{\frac{\Delta l}{L}} \quad (28)$$

Remark 4. As the output angle varies only by 27.8% from first mode to angle limit, whereas the input angle changes sign, it is reasonable to say that the mechanism output is quite decoupled from the input actuation until snap-through occurs, where the output angle suddenly switches. For instance, the input–output decoupling behavior of a pinned–pinned buckled beam has been exploited in the design of a fully compliant handheld tool used for surgical puncturing devices [10].

Fig. 4c presents the strain energy of the beam as a function of the input angle. We can point out two energy minima corresponding to the two stable equilibriums FM1 and FM2 of the bistable mechanism. The energy difference from first mode (FM1 or FM2) to angle limit (AL1 or AL2) corresponds to the actuation energy required to switch state. It also corresponds to the amount of energy released during snap-through. If this energy is not harvested at the mechanism output, the beam will vibrate until the energy is totally damped out. Note that the strain energy at angle limit points is slightly higher than for the second mode (see the zoomed inset in Fig. 4c).

The snapping time (time taken to reach the stable position) and the resonance frequency will depend on the mass density of the beam and the rotary inertia of the output pivot, in addition to the damping of the system [31,32]. If the output pivot inertia is sufficiently high, the snap-through of the buckled beam itself can largely precede the motion of the output pivot.

The beam deflection is computed using Eq. (17) and is plotted in Fig. 4d for the states FM1, FM2, SM1, ML1, AL1 and ZC1 to illustrate the critical shapes of the buckled beam during rotation actuation.

3.3. Fixed–pinned buckled beam

3.3.1. Modeling

We now derive the model of the fixed–pinned buckled beam. Using the boundary conditions $dy/ds(s=0) = 0$ and $y(s=L) = 0$, Eq. (4) gives:

$$C = -\frac{A}{L} kL \quad (29)$$

$$B = -A \frac{kL - \sin(kL)}{1 - \cos(kL)} \quad (30)$$

The fixed–pinned buckled beam deflection becomes:

$$y(s) = A \left[\sin\left(kL \frac{s}{L}\right) - \frac{kL - \sin(kL)}{1 - \cos(kL)} \left(\cos\left(kL \frac{s}{L}\right) - 1 \right) - kL \frac{s}{L} \right] \quad (31)$$

where, from Eqs. (11), (29) and (30):

$$A = \pm 2L \sqrt{\frac{\Delta l}{L} (1 - \cos(kL)) \cdot \left[(kL)^4 - (kL)^3 \left(2 \sin(kL) + \frac{\sin(2kL)}{2} \right) + 2(kL)^2 (\cos(kL) - \cos(2kL)) - kL (2 \sin(kL) - \sin(2kL)) \right]^{-\frac{1}{2}}} \quad (32)$$

The input and output moments can be expressed by substituting the second differentiation of Eq. (31) with respect to s into Eq. (1), yielding:

$$M_{in} = M(s=L) = \frac{EI}{L} \frac{A}{L} (kL)^2 \frac{kL \cos(kL) - \sin(kL)}{1 - \cos(kL)} \quad (33)$$

$$M_{out} = M(s=0) = \frac{EI}{L} \frac{A}{L} (kL)^2 \frac{kL - \sin(kL)}{1 - \cos(kL)} \quad (34)$$

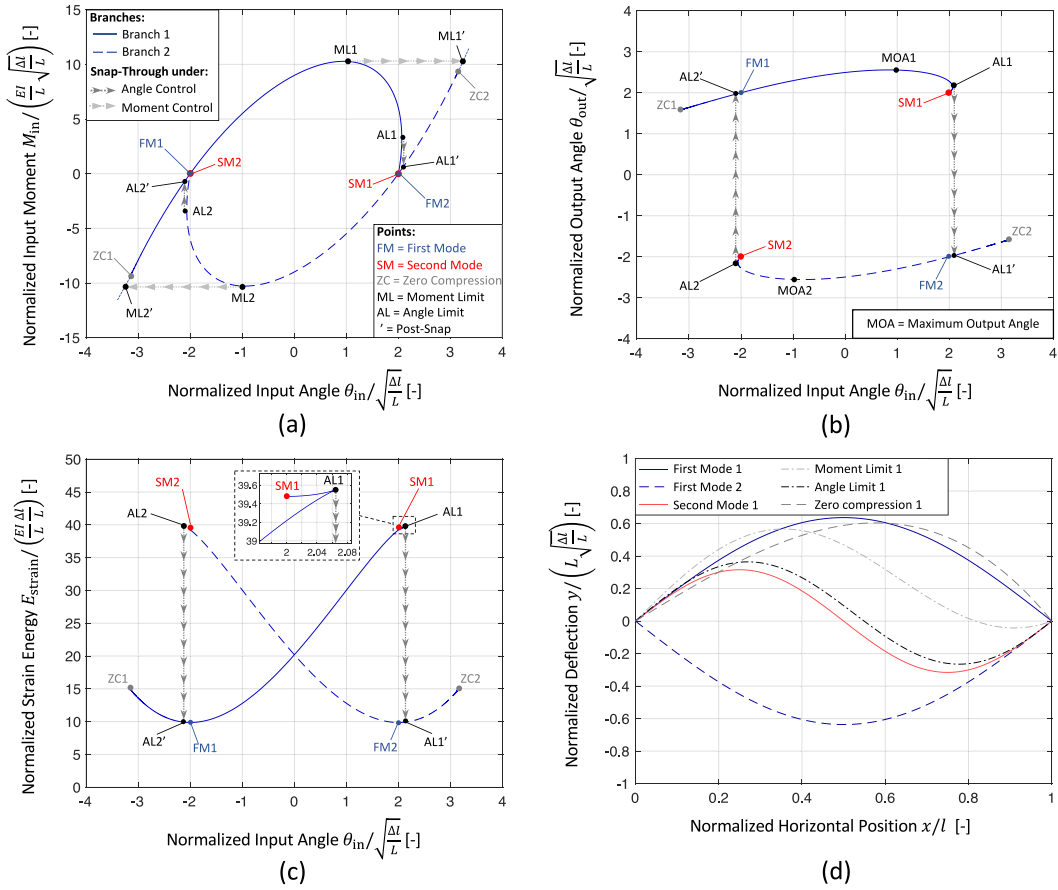


Fig. 4. Normalized actuation characteristics of the pinned–pinned buckled beam actuated in rotation at its right extremity. (a) Input moment versus input angle, (b) output angle versus input angle, (c) beam strain energy versus input angle, and (d) beam deflections at critical points.

Considering $\theta \cong dy/ds$, the input angle follows from differentiating Eq. (31) with respect to s :

$$\theta_{in} = \theta(s = L) = \frac{A}{L} kL \frac{kL \sin(kL) - 2(1 - \cos(kL))}{1 - \cos(kL)} \quad (35)$$

Using Eqs. (29), (30) and (32), the strain energy and the maximum stress can be calculated from Eqs. (12) and (13), respectively:

$$E_{strain} = \frac{1}{4} \frac{EI}{L} \left(\frac{A}{L} \right)^2 \left(\frac{kL}{1 - \cos(kL)} \right)^2 \cdot \left[(kL)^4 - (kL)^3 \left(2 \sin(kL) - \frac{\sin(2kL)}{2} \right) - (kL)^2 (2 \cos(kL) - 1 - \cos(2kL)) + kL (2 \sin(kL) - \sin(2kL)) \right] \quad (36)$$

$$\sigma_{max} = \frac{Eh}{2L} \frac{|A|}{L} \frac{(kL)^2}{1 - \cos(kL)} \cdot \begin{cases} \sin(kL) - kL \cos(kL), & 0 \leq kL < 2.33 \\ \sqrt{(kL)^2 - 2kL \sin(kL) + 2(1 - \cos(kL))}, & kL \geq 2.33 \end{cases} \quad (37)$$

3.3.2. Equilibrium positions

Equilibrium deflections of the fixed–pinned beam are obtained when $M_{in} = 0$ (no external actuation) and $A \neq 0$ (post-buckling deflection from Eq. (31)). Applying these conditions in Eqs. (32) and (33), the parameter kL becomes a solution of the transcendental equation $kL = \tan(kL)$ leading to the following smallest nonzero roots:

$$(kL)_{equi} = 4.49, 7.73, 10.90, \dots \quad (38)$$

As for the pinned–pinned buckled beam, these specific values of kL are called buckling modes where $kL = 4.49$ corresponds to the first buckling mode, $kL = 7.73$ is the second buckling mode, etc. The fixed–pinned buckled beam is also bistable with global minimum energy at the first mode equilibriums (see Eq. (36)). When the beam is stable, i.e., at $kL = 4.49$ (first mode), the input

angle and the output moment magnitudes can be expressed as, respectively, from Eqs. (35) and (34):

$$\theta_{\text{stable}} = 2.49 \sqrt{\frac{\Delta l}{L}} \quad (39)$$

$$M_{\text{stable}} = 8.99 \frac{EI}{L} \sqrt{\frac{\Delta l}{L}} \quad (40)$$

Remark 5. As opposed to the double-pinned case, the input pivot of the fixed-pinned buckled beam has not the same angle magnitude for each mode, see Eqs. (35) and (38).

3.3.3. Actuation characteristics

By actuating the input pivot of the fixed-pinned buckled beam mechanism, we can switch from one stable state to the other. The actuation characteristics are plotted in Fig. 5. The parametric curves of the input moment (Eq. (33)), the output moment (Eq. (34)) and the strain energy (Eq. (36)) as a function of the input angle (Eq. (35)) are plotted in Figs. 5a, 5b and 5c, respectively. The free parameter kL is varied from 0 (no compressive force) to 7.73 (second mode). The two symmetrical branches (Branch 1 and Branch 2) are displayed to characterize the snap-through of the beam due to moment or angle controls. As in the pinned-pinned case, the second and higher modes are never reached due to input moment limits (ML1 and ML2) and angle limits (AL1 and AL2) encountered before the second mode points (SM1 and SM2). The magnitudes of the moment and angle limit points are:

$$M_{\text{in,lim}} = 12.90 \frac{EI}{L} \sqrt{\frac{\Delta l}{L}} \quad (41)$$

$$\theta_{\text{in,lim}} = 1.78 \sqrt{\frac{\Delta l}{L}} \quad (42)$$

at $kL = 6.49$ and at $kL = 7.59$, respectively.

Compared to the double-pinned configuration, the points ML1' and ML2' are contained within Branch 2 and Branch 1 respectively, see Figs. 4a and 5a, meaning that the beam is still in compression after snap-through under moment control. Another difference is that the input pivot angle has a larger magnitude at the first modes FM1 and FM2 than at the angle limit points AL1 and AL2, see Eqs. (39) and (42). This means that the input angle can continuously increase to pass from FM1 to FM2 (following the path FM1—ML1—AL1—AL1'—FM2) and continuously decrease to come back to FM1 (through FM2—ML2—AL2—AL2'—FM1).

When angle control is used to switch state, Fig. 5b shows that the output moment magnitude continuously increases and reaches a maximum value at the angle limit points AL1 and AL2. This maximum output moment magnitude is equal to:

$$M_{\text{out,max}} = 15.31 \frac{EI}{L} \sqrt{\frac{\Delta l}{L}} \quad (43)$$

The output moment magnitude increases thus by 70.3% from first mode to angle limit point, see Eqs. (40) and (43). After snap-through, the output reaction moment is suddenly reversed.

Fig. 5c presents the strain energy of the beam as a function of the input angle. The bistability of the mechanism is noticed from the two energy minima at the first mode points FM1 and FM2. The strain energy difference from first mode to angle limit point corresponds to the required actuation energy to switch state. During snap-through, this energy will be damped during the vibration of the beam, since the output, considered fixed, cannot harvest energy. Alternatively, the snap-through energy can be harvested by a piezoelectric film attached on the top or bottom surface of the beam [33].

The deflected shape of the beam is computed using Eqs. (3) and (31) for the critical states FM1, FM2, SM1, ML1, AL1 and ZC1, and plotted in Fig. 5d.

Remark 6. As seen in Figs. 4a and 5a, the second buckling mode is stable for small input angle disturbances since the tangent stiffness is positive. However, those structures are unstable in second mode shape, as small disturbances applied laterally to the beam lead to instability [34].

Remark 7. In this article, we derived a generic model for a slender beam under compression. However, by rotating its input beyond the zero compression points ZC1 and ZC2 (see Figs. 4 and 5), the beam becomes subjected to tension. This case can be treated with the presented model, by defining kL as an imaginary number (since $P < 0$ in Eq. (5)).

4. Validation of the analytical model

4.1. Material and methods

In order to verify the accuracy of the analytical model derived in Section 3, we conduct a finite element analysis and a physical experiment on a buckled beam with parameters listed in Table 1. Both pinned-pinned and fixed-pinned configurations of the buckled beam are evaluated. As material for the elastic beam, spring steel (1.1274) was chosen for its high ratio of yield strength to Young's modulus (σ_y/E). The beam has a high slenderness ratio of $L/h = 800$, as assumed in the theoretical model. Since the angle limit is always encountered after the moment limit (see Figs. 4a and 5a), angle control is selected to characterize the entire snap-through behavior. Three different precompression displacements are tested (see Table 1), allowing to validate our model on different levels of beam deformation.

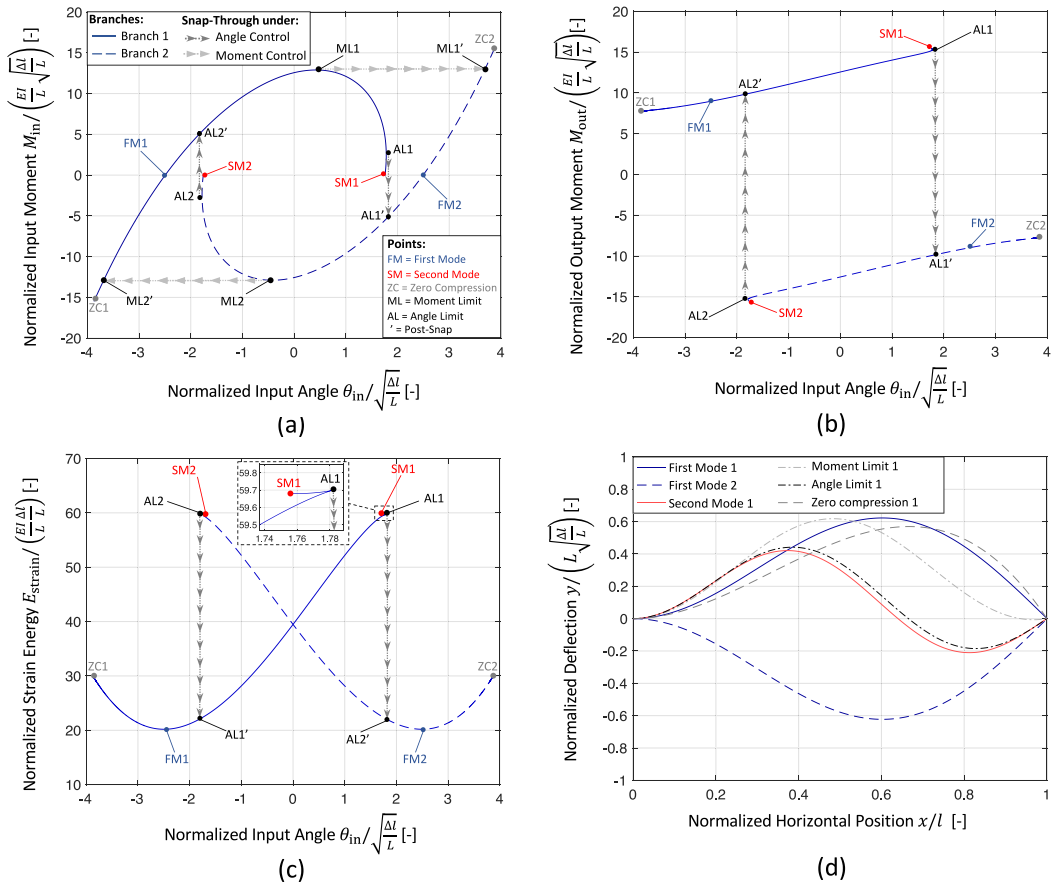


Fig. 5. Normalized actuation characteristics of the fixed-pinned buckled beam actuated in rotation at its right extremity. (a) Input moment versus input angle, (b) output moment versus input angle, (c) beam strain energy versus input angle, and (d) beam deflections at critical points.

Table 1
Design parameters of the buckled beam.

	Parameter	Value
Material (spring steel 1.1274)	E	210 GPa
	σ_y	1600 MPa
Beam dimensions	h	0.25 mm
	b	25 mm
	L	200 mm
Precompression displacements	Δl	3 mm
		5 mm
		7.5 mm

4.2. Finite element method

A 2D stationary FEM simulation is conducted using the commercial software COMSOL Multiphysics 5.6 in order to verify the theoretical model. The beam with dimensions stated in Table 1 is meshed with quadrilateral shell elements such that 4 elements are mapped across its thickness h and 3200 elements along its length L . The material parameters are taken from Table 1 and the Poisson's ratio is set to zero (since Poisson effects are neglected in the analytical model). The stationary solver uses the Solid Mechanics module to simulate the deformation of the beam. The Geometric Nonlinearity setting is selected to capture large deformation, buckling and snap-through behaviors. The Segregated approach is adopted to speed up the convergence of the stationary solver.

Two rigid connectors attached at each beam end are used to define the boundary conditions (pinned-pinned or fixed-pinned), the precompression displacement, and to actuate the right extremity with an incremental angle. For each actuating angle, the study reuses the previous solution, allowing to stay on the same branch until the angle limit point causes a branch jump.

For each boundary condition and each precompression displacement, the following results are exported: the input angle, the input moment, the strain energy of the beam and the maximum von Mises stress in the beam. Depending on the boundary condition, the output angle or the output reaction moment is evaluated. These FEM results are presented and compared to the analytical model in Section 5.

Remark 8. It can happen that FEM models predict higher buckling modes than expected in practice. This can be avoided by using small bias forces applied laterally to the beam or initial imperfections to force the FEM solver to choose a direction of buckling and thus remove such unrealistic modes [15,17,35]. In our case, as we imposed an angle to the input pivot at the same time as the preload, a buckling direction was already selected by the solver and no perturbation was needed.

4.3. Experimental method

An experimental study was carried out to validate that the snap-through behaviors predicted by the theoretical and FEM models also happen in practice. Using the test bench shown in Fig. 6, a series of experiments were conducted to verify the nonlinear moment–angle characteristics of the input and output pivots. The experimental setup consists of a beam (with properties specified in Table 1) pinned at each end using two pivots. In order to limit friction, the pivots are implemented using ball bearings whose axes coincide with the extremities of the beam. The bearing axes are also parallel to the direction of gravity in order to minimize gravity-related effects. Rigid levers are fixed to each beam extremity to transform input and output angles and moments into linear displacements and forces that can be controlled and measured via the setup. In such manner, a displacement sensor (Keyence Model LK-H082) is used to measure the angle of the output pivot and two lateral linear stages are used to actuate the pivots independently and measure the reaction forces using force sensors (Kistler Model 9207 with force introducing cap No. 3.220.139). Note that these are directly measured on the sides of the beam part clamped inside the lever, using lateral slots (see Fig. 6). Before testing, these force sensors were calibrated to ensure a high measurement accuracy. Two axial linear stages are used to move the pivots independently along the beam axis. The one at the output pivot is used to adjust the distance between the output bearing axis and the laser beam of the displacement sensor. The other axial guide is used to set the precompression displacement.

At the start of the experiment, the beam is precompressed to one of the three preloadings defined in Table 1. The fixed–pinned configuration is obtained by constraining the output lever angle to zero (verified with the laser displacement sensor) using the output lateral linear stage. In the pinned–pinned configuration, the output lateral stage is separated from the output lever to leave it free to rotate. For both boundary conditions scenarios, the measurements start at stable positions (Figs. 7a and 8a for pinned–pinned and fixed–pinned tests, respectively). In practice, the input force sensor cap is just in contact with the input lever, but no reaction force is measured. The input lever angle is then increased gradually using the input lateral stage. At each input angle increment, the input and output moments are obtained from the force sensor readings and the output angle is measured by the laser sensor. All measurements are taken when the system is at static equilibrium to avoid dynamic effects. Some measurements are taken after the snap-through for the pinned–pinned condition. However, for the fixed–pinned case, the experiment stops when the beam snaps since the output force sensor loses contact with the output lever. The experimental results are compared to the analytical and FEM models in Section 5. The uncertainty of the measurements (not shown on the graphs of Figs. 9–12 to preserve readability), corresponds to ± 1.3 deg for the input angle, ± 0.6 deg for the output angle, ± 4 Nmm for the input and output moments, and ± 10 μm for the end-shortening.

Remark 9. This experimental setup only allows to actuate the input lever with a positive moment, which means that only one actuation path can be characterized. However, given the symmetry of the mechanisms, the characteristics and behaviors should be symmetrical and developing a test bench with input moment in both directions is not required.

5. Results and discussions

In this section, the results of the analytical model, the FEM simulation and the experimental study are presented and discussed. In Section 5.1, we show and compare the actuation characteristics of the pinned–pinned and fixed–pinned buckled beams. Section 5.2 compares the analytical values of angles and moments at the critical points against FEM and experimental data, for different levels of beam preloading. Possible discrepancies between the results allow to evaluate the accuracy of the analytical model presented in this paper.

5.1. Actuation characteristics

Analytical model, FEM and experimental results are presented together for the actuation characteristics of the pinned–pinned and fixed–pinned buckled beams in Figs. 9 and 10, respectively. For each configuration, we display the input moment, the beam strain energy, the output angle (for the pinned–pinned buckled beam) or the output moment (for the fixed–pinned buckled beam), and the maximum stress in the beam.

Figs. 9 and 10 show that the proposed model successfully predicts the key characteristics of the buckled beam actuation as the analytical results are consistent with the FEM and the experimental data. The maximum stress graphs (Figs. 9d and 10d) show that the material yield strength σ_y (stated in Table 1) is not exceeded for the whole actuation.

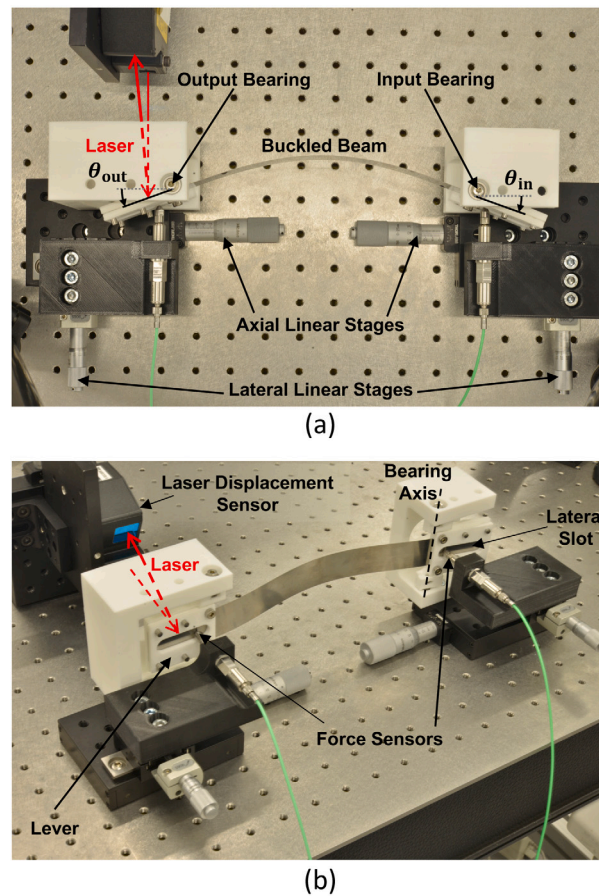


Fig. 6. Test bench used to characterize the switching behavior of the pinned–pinned and fixed–pinned buckled beams: (a) top view, and (b) perspective view.

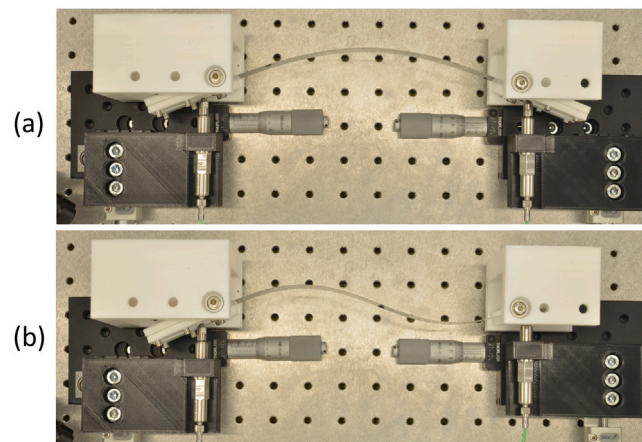


Fig. 7. Actuation tests of the buckled beam with pinned–pinned boundary conditions. The buckled beam is shown in (a) stable position and (b) in angle limit position.

It can be observed that the pinned–pinned and fixed–pinned bistable buckled beams have nearly the same behaviors under angle control, namely:

1. The actuation characteristics involves two symmetrical branches.
2. To switch from one branch to the other, the magnitude of the input moment always reaches a maximum.
3. The beam snaps at an angle limit point before reaching its second buckling mode.
4. The output angle and moment are essentially decoupled from the input actuation until snap-through occurs, where the output angle and moment suddenly change sign.

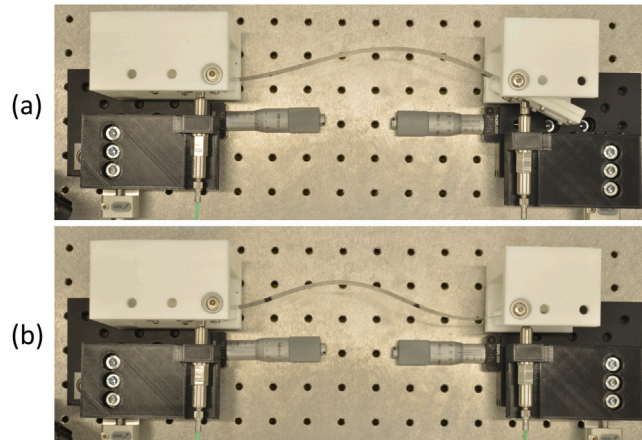


Fig. 8. Actuation tests of the buckled beam with fixed-pinned boundary conditions. The buckled beam is shown in (a) stable position and (b) in angle limit position.

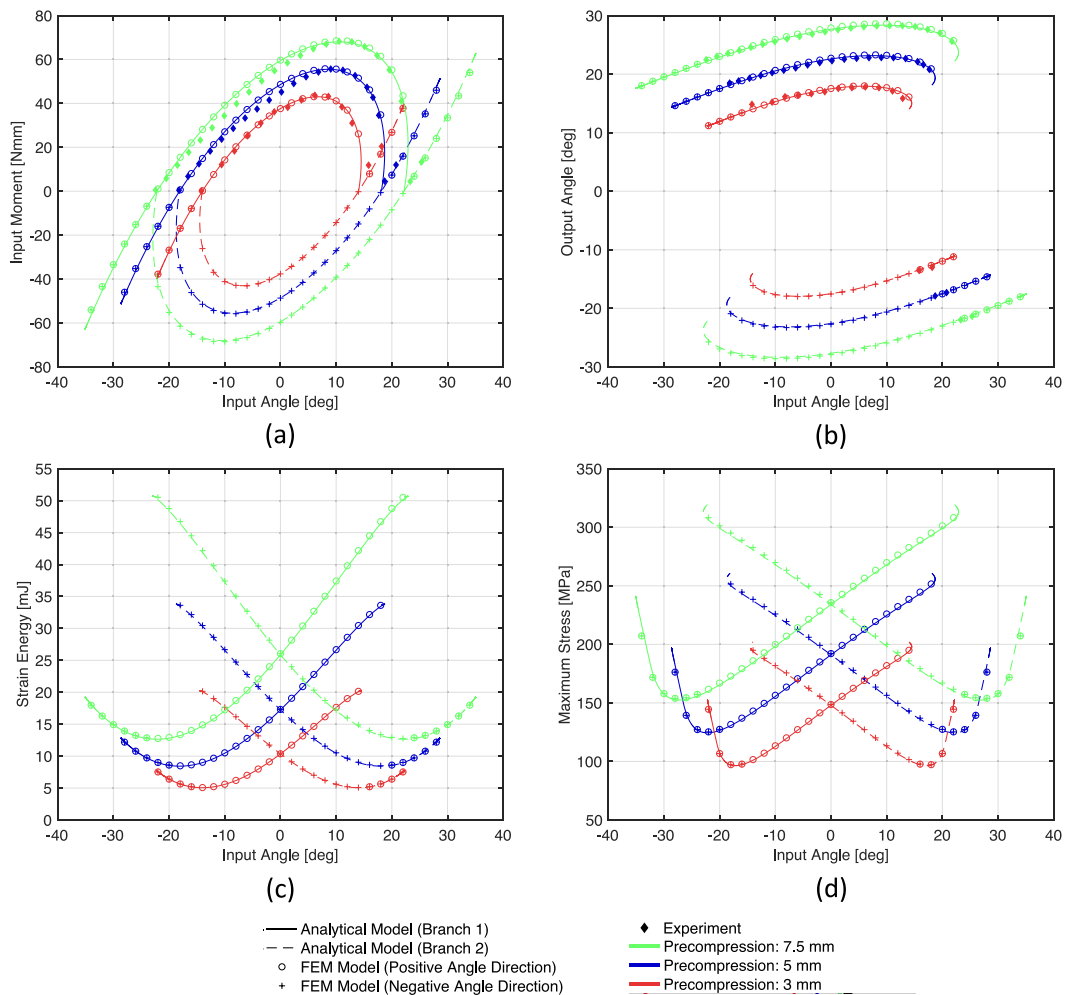


Fig. 9. Pinned-pinned buckled beam actuation characteristics as a function of the input angle: (a) input moment, (b) output angle, (c) strain energy, and (d) maximum stress. See Fig. 4 for the position of the critical points.

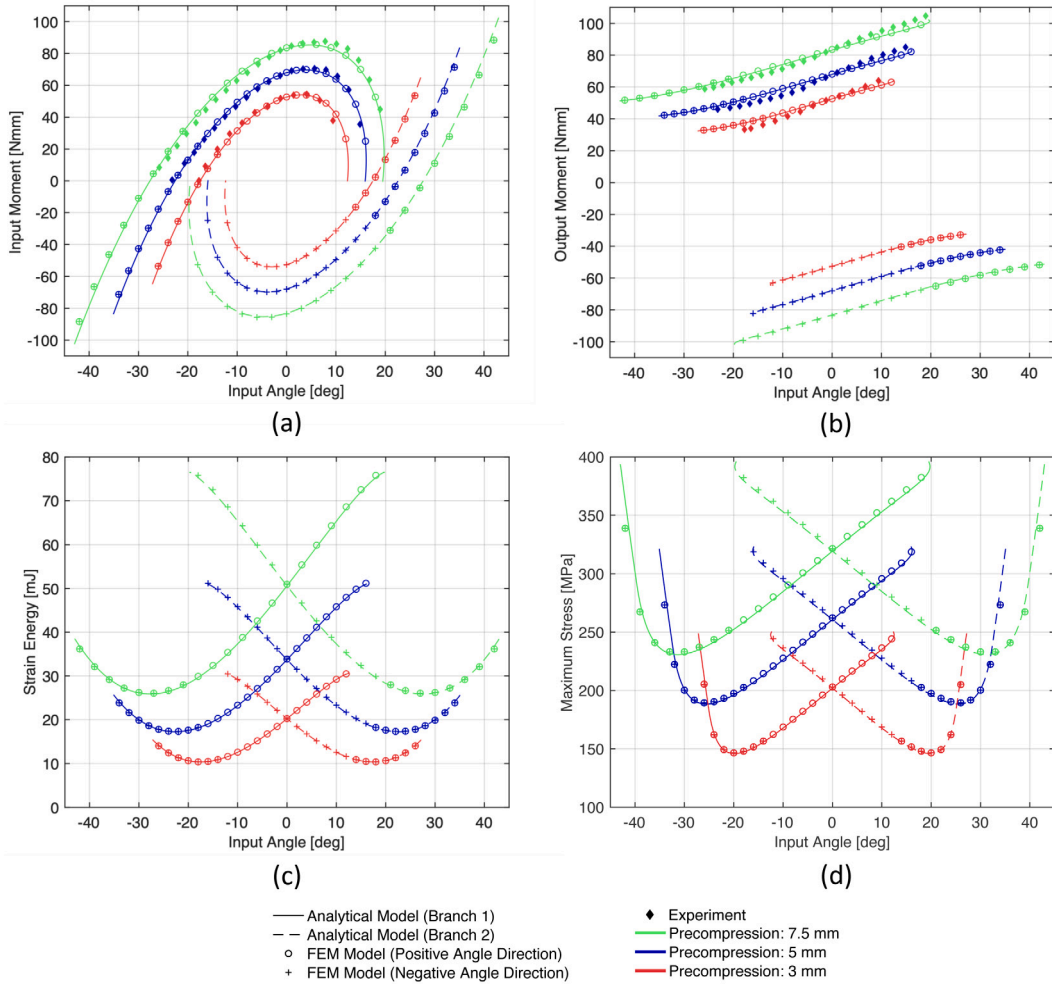


Fig. 10. Fixed-pinned buckled beam actuation characteristics as a function of the input angle: (a) input moment, (b) output moment, (c) strain energy, and (d) maximum stress. See Fig. 5 for the position of the critical points.

A major difference is that the first mode input angle θ_{stable} is smaller in magnitude than the input angle limit $\theta_{in,lim}$ for the pinned-pinned buckled beam (see Figs. 4a and 9a), whereas it is the opposite for the fixed-pinned buckled beam (see Figs. 5a and 10a). In the case of the fixed-pinned buckled beam, this leads to a change in sign for the input moment when the beam snaps under angle control. In the case of the double-pinned buckled beam, this means that the input angle magnitude must be decreased after snap-through under angle control for the beam to come back to its stable position.

In terms of power consumption to switch state for the same precompression displacement, compared to the fixed-pinned case, the pinned-pinned buckled beam needs a lower input moment magnitude ($\sim 20\%$ lower from Eqs. (26) and (41)) and less input energy ($\sim 25\%$ lower from Figs. 4c and 5c), but has a lower stable angle stroke ($\sim 20\%$ lower from Eqs. (25) and (39)).

Compared to force actuation, where snap-through of pinned-pinned and fixed-pinned buckled beams occurs at second mode [34], this paper shows that moment actuation requires slightly more energy (see insets in Figs. 4c and 5c). Another difference is the constant negative stiffness region demonstrated for pinned-pinned buckled beams under central actuating force [18], which is not observed here. Actually, moment actuation shares similarities with off-center force actuation: two distinct symmetrical branches and energy jumps to switch between them [18].

5.2. Critical angles and moments

The critical angles and moments correspond to the input and output angles and moments encountered at the critical points of the actuation characteristics. Their analytical expressions (derived in Sections 3.2 and 3.3) are important as they are key actuation parameters to design such buckled beams. These values are compared with FEM and experimental results in Figs. 11 and 12, as a function of its precompression rate $\Delta l/L$, for pinned-pinned and fixed-pinned buckled beams, respectively.

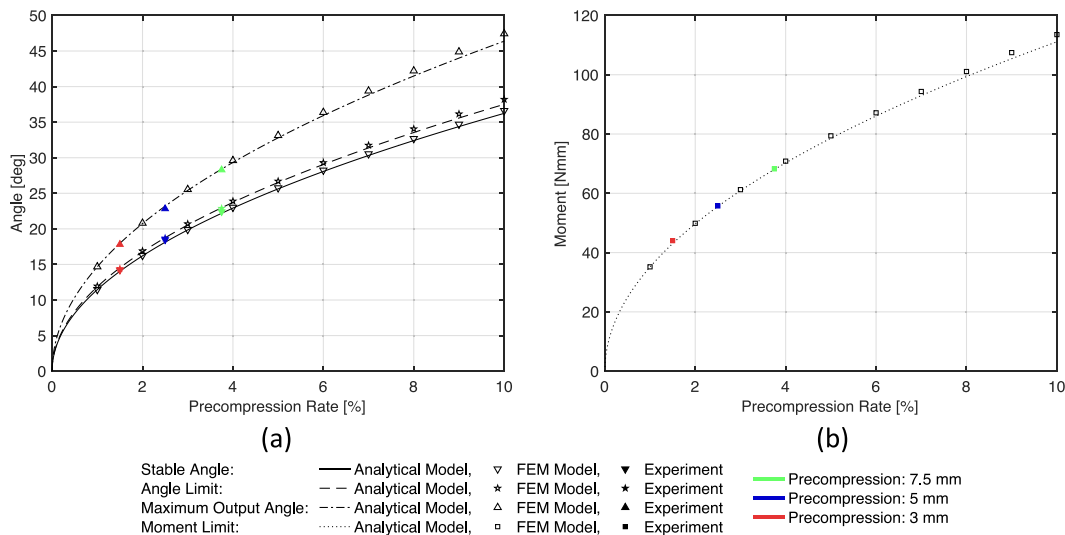


Fig. 11. Pinned-pinned buckled beam critical angles (a) and moments (b) as a function of the precompression rate.

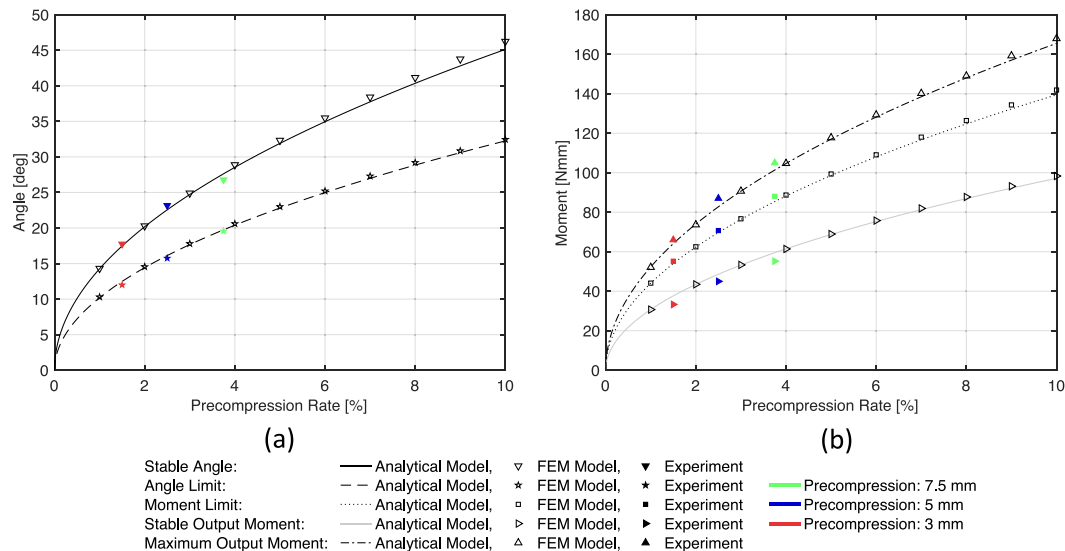


Fig. 12. Fixed-pinned buckled beam critical angles (a) and moments (b) as a function of the precompression rate.

We can observe in these figures, that the results from our analytical model are consistent with the FEM and experimental data. Indeed, for both pinned-pinned and fixed-pinned configurations, the relative errors between the simulation results and the analytical model are bounded within 2.5%. The error between the analytical curve and the FEM data has the tendency to increase when increasing the beam precompression (as it can be observed in Figs. 11 and 12). This can be attributed to the small deformation assumption of our analytical model, which begins to leave its domain of validity. For higher deformations of the beam, it becomes necessary to adopt numerical models to evaluate the actuation characteristics with acceptable precision.

The major discrepancy between experimental data and the model is observed in the stable and maximum output moments (see Fig. 12b), where the relative error is bounded within 12%. These divergences between the theoretical and experimental results can be attributed to manufacturing and assembly tolerances, small predeformations of the beam, and friction in the bearings of the test bench.

6. Example of application and design guidelines

In order to show the practical potential of the mechanisms described in this article and to demonstrate the strength of our analytical model, we give an example of its application on a novel bistable gripper. This mechanism presented in Fig. 13 uses the

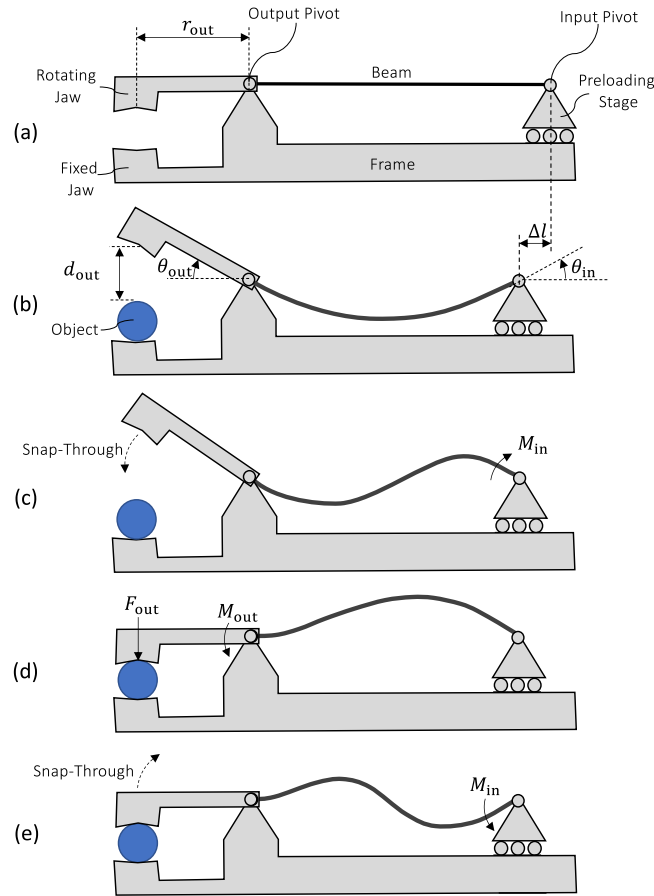


Fig. 13. Schematic of a bistable gripper based on a preloaded buckled beam. (a) The gripper mechanism is shown as-fabricated. (b) The buckled beam is precompressed by the preloading stage in stable open position (the beam boundaries are in this case pinned–pinned). (c) The output state switches from open to closed using an input actuation. (d) The gripper is in stable closed position (boundaries of the beam are hence fixed–pinned). (e) The output state switches from closed to open using a reverse input actuation.

snap-through behavior of a buckled beam sustained by two pivots to grab and release an object via a rotating jaw placed at the output pivot. The change of state between “open” and “closed” is performed using a rotating actuator at the input pivot.

Note that the open and closed states correspond respectively to the pinned–pinned and fixed–pinned configurations of the buckled beam. Hence, the theoretical model derived in this paper can be used to design this bistable gripper for given gripping and actuation specifications. For instance, in open and closed stable positions, the jaw stroke d_{out} (Fig. 13b) and the gripping force F_{out} (Fig. 13d) are given by Eqs. (25) and (40), respectively:

$$d_{out,stable} = r_{out} \theta_{out,stable} = 2r_{out} \sqrt{\frac{\Delta l}{L}} \quad (44)$$

$$F_{out,stable} = \frac{M_{out,stable}}{r_{out}} = 8.99 \frac{EI}{L} \sqrt{\frac{\Delta l}{L}} \frac{1}{r_{out}} \quad (45)$$

To switch the gripper state, the input actuator must provide enough torque M_{in} to overpass the input moment limit $M_{in,lim}$ for both pinned–pinned and fixed–pinned cases, expressed in Eqs. (26) and (41), respectively. The actuator angular stroke θ_{in} needs to be sufficiently large to overpass the angle limits $\theta_{in,lim}$ for the pinned–pinned and fixed–pinned configurations given by Eqs. (27) and (42), respectively. Finally, using Eqs. (23) and (37), we can verify that the maximum stress in the beam does not exceed the material yield strength during the actuation.

Due to its bistable and snap-through behaviors, this novel gripper mechanism has many advantages, namely:

1. No power is required from the actuator to keep the stable output states (open and closed).
2. Very fast switching is obtained due to beam snap-through.
3. The static output force is limited to a maximum value (see Eq. (43)), preventing damaging the object.
4. The preloading stage allows to adjust the precompression, thus the stable output stroke and the gripping force according to Eqs. (44) and (45).

7. Conclusion and perspectives

In this article, we proposed to actuate pinned–pinned and fixed–pinned bistable buckled beams using a rotation at one of their extremities. By means of a new analytical model, we established normalized graphs and closed-form expressions that allow to efficiently design these bistable mechanisms. The consistency of the theoretical results with FEM and experimental data, confirmed both the validity and the high accuracy of our model. The practicality of the new mechanisms and model was illustrated on a novel gripper concept. As the proposed theoretical approach derived in Section 3.1 is generic, it can be next applied to a wide variety of mechanisms based on preloaded beams with different boundary conditions and actuations.

Our future research will evaluate the extension of the bistable gripper design of Section 6 to include an actuator based on agonist–antagonist shape memory alloys (SMA). These have the advantage of being compact and lightweight, and only needing to be activated to switch between the two stable states [36]. Additionally, the input and output pivots could be implemented with flexures in order to make the mechanism monolithic and thus manufacturable at microscale for MEMS applications, e.g., micro-manipulation [37]. The presented analytical model would hence have to be adapted to take into account angular stiffnesses at the boundary conditions. Finally, it would be worthwhile studying the vibratory behavior of such buckled beam mechanisms during the transition between stable states.

Declaration of competing interest

The authors declare that they have no known competing financial interests or personal relationships that could have appeared to influence the work reported in this paper.

References

- [1] M.P. Brenner, J.H. Lang, J. Li, J. Qiu, A.H. Slocum, Optimal design of a bistable switch, *Proc. Natl. Acad. Sci.* 100 (17) (2003) 9663–9667, <http://dx.doi.org/10.1073/pnas.1531507100>.
- [2] H. Sattari, A. Toros, T. Grazioli, N. Quack, Bistable silicon photonic MEMS switches, in: W. Piyawattanametha, Y.-H. Park, H. Zappe (Eds.), in: *MOEMS and Miniaturized Systems XVIII*, vol. 10931, International Society for Optics and Photonics, SPIE, 2019, pp. 97–104, <http://dx.doi.org/10.1117/12.2507192>.
- [3] C. Goll, W. Bacher, B. Bustgens, D.J. Maas, W. Menz, W.K. Schomburg, Microvalves with bistable buckled polymer diaphragms, *J. Micromech. Microeng.* 6 (1996) 77–79, <http://dx.doi.org/10.1088/0960-1317/6/1/017>.
- [4] B. Charlot, W. Sun, K. Yamashita, H. Fujita, H. Toshiyoshi, Bistable nanowire for micromechanical memory, *J. Micromech. Microeng.* 18 (4) (2008) 045005, <http://dx.doi.org/10.1088/0960-1317/18/4/045005>.
- [5] D. Pan, Z. Wu, F. Dai, N. Tolou, A novel design and manufacturing method for compliant bistable structure with dissipated energy feature, *Mater. Des.* 196 (2020) 109081, <http://dx.doi.org/10.1016/j.matdes.2020.109081>.
- [6] M.T.A. Saif, On a tunable bistable MEMS-theory and experiment, *J. Microelectromech. Syst.* 9 (2) (2000) 157–170, <http://dx.doi.org/10.1109/84.846696>.
- [7] B. Demiralp, H.S. Pisheh, B. Kucukoglu, U. Hatipoglu, M.S. Hanay, Monitoring micromechanical buckling at high-speed for sensing and transducer applications, in: 2021 21st International Conference on Solid-State Sensors, Actuators and Microsystems (Transducers), IEEE, 2021, pp. 627–630, <http://dx.doi.org/10.1109/Transducers50396.2021.9495591>.
- [8] P.R. Kuppens, J.L. Herder, N. Tolou, Permanent stiffness reduction by thermal oxidation of silicon, *J. Microelectromech. Syst.* 28 (5) (2019) 900–909, <http://dx.doi.org/10.1109/JMEMS.2019.2935379>.
- [9] J. Qiu, J.H. Lang, A.H. Slocum, A curved-beam bistable mechanism, *J. Microelectromech. Syst.* 13 (2) (2004) 137–146, <http://dx.doi.org/10.1109/JMEMS.2004.825308>.
- [10] M. Zanaty, T. Fussinger, A. Rogg, A. Lovera, D. Lambelet, I. Vardi, T.J. Wolfensberger, C. Baur, S. Henein, Programmable multistable mechanisms for safe surgical puncturing, *J. Med. Devices* 13 (2) (2019) <http://dx.doi.org/10.1115/1.4043016>.
- [11] Y. Gerson, S. Krylov, B. Ilic, D. Schreiber, Design considerations of a large-displacement multistable micro actuator with serially connected bistable elements, *Finite Elem. Anal. Des.* 49 (1) (2012) 58–69, <http://dx.doi.org/10.1016/j.finel.2011.08.021>.
- [12] M. Vangbo, An analytical analysis of a compressed bistable buckled beam, *Sensors Actuators A* 69 (3) (1998) 212–216, [http://dx.doi.org/10.1016/S0924-4247\(98\)00097-1](http://dx.doi.org/10.1016/S0924-4247(98)00097-1).
- [13] P. Cazottes, A. Fernandes, J. Pouget, M. Hafez, Bistable buckled beam: Modeling of actuating force and experimental validations, *J. Mech. Des.* 131 (10) (2009) <http://dx.doi.org/10.1016/j.ijsolstr.2014.01.017>.
- [14] H. Hussein, P. Le Moal, G. Bourbon, Y. Haddab, P. Lutz, Modeling and stress analysis of a pre-shaped curved beam: Influence of high modes of buckling, *Int. J. Appl. Mech.* 7 (04) (2015) 1550055, <http://dx.doi.org/10.1142/S1758825115500556>.
- [15] W. Yan, Y. Yu, A. Mehta, Analytical modeling for rapid design of bistable buckled beams, *Theor. Appl. Mech. Lett.* 9 (4) (2019) 264–272, <http://dx.doi.org/10.1016/j.taml.2019.04.006>.
- [16] J. Zhao, J. Jia, X. He, H. Wang, Post-buckling and snap-through behavior of inclined slender beams, *J. Appl. Mech.* 75 (4) (2008) <http://dx.doi.org/10.1115/1.2870953>.
- [17] G.L. Holst, G.H. Teichert, B.D. Jensen, Modeling and experiments of buckling modes and deflection of fixed-guided beams in compliant mechanisms, *J. Mech. Des.* 133 (5) (2011) <http://dx.doi.org/10.1115/1.4003922>.
- [18] B. Camescasse, A. Fernandes, J. Pouget, Bistable buckled beam: Elastica modeling and analysis of static actuation, *Int. J. Solids Struct.* 50 (19) (2013) 2881–2893, <http://dx.doi.org/10.1016/j.ijsolstr.2013.05.005>.
- [19] B. Camescasse, A. Fernandes, J. Pouget, Bistable buckled beam and force actuation: Experimental validations, *Int. J. Solids Struct.* 51 (9) (2014) 1750–1757, <http://dx.doi.org/10.1016/j.ijsolstr.2014.01.017>.
- [20] L. Tissot-Daguette, C. Baur, A. Bertholds, P. Llosas, S. Henein, Design and modelling of a compliant constant-force surgical tool for objective assessment of ossicular chain mobility, in: 2021 21st International Conference on Solid-State Sensors, Actuators and Microsystems (Transducers), IEEE, 2021, pp. 1299–1302, <http://dx.doi.org/10.1109/Transducers50396.2021.9495605>.
- [21] L. Tissot-Daguette, M. Smreczak, C. Baur, S. Henein, Load cell with adjustable stiffness based on a preloaded T-shaped flexure pivot, in: Euspen's 21st International Conference & Exhibition, Copenhagen, DK, June 2021, 2021, pp. 217–220.
- [22] A. Yamada, M. Watari, H. Mochiyama, H. Fujimoto, An asymmetric robotic catapult based on the closed elastica for jumping robot, in: 2008 IEEE International Conference on Robotics and Automation, IEEE, 2008, pp. 232–237, <http://dx.doi.org/10.1109/ROBOT.2008.4543214>.
- [23] A. Zhang, G. Chen, A comprehensive elliptic integral solution to the large deflection problems of thin beams in compliant mechanisms, *J. Mech. Robot.* 5 (2) (2013) <http://dx.doi.org/10.1115/DETC2012-70239>.

- [24] J.-S. Chen, S.-Y. Hung, Snapping of an elastica under various loading mechanisms, *Eur. J. Mech. A Solids* 30 (4) (2011) 525–531, <http://dx.doi.org/10.1016/j.euromechsol.2011.03.006>.
- [25] J.-S. Chen, Y.-H. Su, On the use of an elastica-slider assembly as a bistable device, *Mech. Mach. Theory* 49 (2012) 40–51, <http://dx.doi.org/10.1016/j.mechmachtheory.2011.11.008>.
- [26] J. Beharic, T.M. Lucas, C.K. Harnett, Analysis of a compressed bistable buckled beam on a flexible support, *J. Appl. Mech.* 81 (8) (2014) <http://dx.doi.org/10.1115/1.4027463>.
- [27] P.S. Harvey Jr., L.N. Virgin, Coexisting equilibria and stability of a shallow arch: Unilateral displacement-control experiments and theory, *Int. J. Solids Struct.* 54 (2015) 1–11, <http://dx.doi.org/10.1016/j.ijsolstr.2014.11.016>.
- [28] J. Cleary, H.-J. Su, Modeling and experimental validation of actuating a bistable buckled beam via moment input, *J. Appl. Mech.* 82 (5) (2015) 051005, <http://dx.doi.org/10.1115/1.4030074>.
- [29] H. Hussein, M.I. Younis, Analytical study of the snap-through and bistability of beams with arbitrarily initial shape, *J. Mech. Robot.* 12 (4) (2020) <http://dx.doi.org/10.1115/1.4045844>.
- [30] S. Palathingal, G.K. Ananthasuresh, Design of bistable pinned-pinned arches with torsion springs by determining critical points, in: X. Zhang, N. Wang, Y. Huang (Eds.), *Mechanism and Machine Science*, Springer Singapore, Singapore, 2017, pp. 677–688, http://dx.doi.org/10.1007/978-981-10-2875-5_56.
- [31] M. Gomez, D. Moulton, D. Vella, Critical slowing down in purely elastic ‘snap-through’ instabilities, *Nat. Phys.* 13 (2017) 142–145, <http://dx.doi.org/10.1038/nphys3915>.
- [32] J.-S. Chen, W.-C. Ro, Dynamic response of a shallow arch under end moments, *J. Sound Vib.* 326 (2009) 321–331, <http://dx.doi.org/10.1016/j.jsv.2009.05.002>.
- [33] Y. Fan, M.H. Ghayesh, T.-F. Lu, A broadband magnetically coupled bistable energy harvester via parametric excitation, *Energy Convers. Manage.* 244 (2021) 114505, <http://dx.doi.org/10.1016/j.enconman.2021.114505>.
- [34] R.H. Plaut, Snap-through of arches and buckled beams under unilateral displacement control, *Int. J. Solids Struct.* 63 (2015) 109–113, <http://dx.doi.org/10.1016/j.ijsolstr.2015.02.044>.
- [35] A. Numić, T.W.A. Blad, F. van Keulen, Effect of matching buckling loads on post-buckling behavior in compliant mechanisms, in: *International Design Engineering Technical Conferences and Computers and Information in Engineering Conference*, Volume 8A: 45th Mechanisms and Robotics Conference (MR), ASME, 2021, <http://dx.doi.org/10.1115/DETC2021-68439>, V08AT08A010.
- [36] P. Motzki, S. Seelecke, Bi-stable SMA actuator, in: *Actuator 16–15th International Conference on New Actuators*, 2016, pp. 317–320, <http://dx.doi.org/10.13140/RG.2.2.12065.20325>.
- [37] Z. Zhang, X. Wang, J. Liu, C. Dai, Y. Sun, Robotic micromanipulation: Fundamentals and applications, *Annu. Rev. Control Robot. Auton. Syst.* 2 (2019) 181–203, <http://dx.doi.org/10.1146/annurev-control-053018-023755>.